AIAA'88

AIAA-88-0619

Solution of Steady Three-Dimensional Compressible Euler and Navier-Stokes Equations by an Implicit LU Scheme

Herbert Rieger
Dornier Gmbh, Friedrichshafen, F.R.G.
Antony Jameson
Princeton Univ., Princeton, NJ

AIAA 26th Aerospace Sciences Meeting
January 11-14, 1988/Reno, Nevada

SOLUTION OF STEADY THREE-DIMENSIONAL COMPRESSIBLE EULER AND NAVIER-STOKES EQUATIONS BY AN IMPLICIT LU SCHEME

by

Herbert Rieger
Dornier GmbH , Aerodynamics Dept. BF30
D-7990 Friedrichshafen 1 , Federal Republic of Germany

and

Antony Jameson
Department of Mechanical and Aerospace Engineering
Princeton University , Princeton , NJ 08544

Abstract

An implicit LU-scheme developed by the second author is modified and extended to three dimensions. The resulting scheme is applied to the solution of the steady compressible Euler and Navier-Stokes equations in the framework of a finite-volume discretization technique.

The approach can be viewed as a deferred-correction solution method, where the implicit operator only approximates the corresponding flux jacobians to first order in space, whereas the central-differenced explicit operators are chosen to be second order accurate on a sufficient smooth grid system. However, the LU-factors have the property of diagonal dominance and therefore are well conditioned allowing a relaxation type solution of the steady equation set.

Results will be presented for some viscous and inviscid subsonic, transonic and hypersonic flow problems.

Introduction

Most of the methods for numerical solution of the steady-state compressible conservation laws are based on time-marching integration procedures.

In implicit schemes the time coordinate is mostly used as a means to provide some sort of diagonal dominance in the coefficient matrices which result after discretization of the implicit operator chosen.

In advanced explicit methods time and space discretization have been separated to allow the application of efficient integration schemes developed for ordinary differential equations. Especially the class of one step multistage schemes, proposed and developed by Jameson [1] for systems of partial differential equations have been proven to perform extremely effective for solving the Euler equations. The original stability limits have been extended considerably by tailoring corresponding integration coefficients and by introducing some implicitness through a residual averaging procedure [2] . Also for the solutions of the Navier-Stokes equations these types of explicit schemes are very promising lines of development.

Without using the time coordinate in implicit schemes diagonal dominance can also be assured by suitable implicit operators, which in general however possess a worse discretization error compared to that the method is designed. This feature leads almost automatically to an approximate Newton-iteration method, where the stable implicit operator only approximates the true jacobians to some lower order.

In this context there are some reasons considering approximate LU decomposition schemes as promising methods for the numerical solution of the three-dimensional Euler and Navier-Stokes equations. In contrast to the alternate direction approach for approximate factorization of the corresponding three-dimensional implicit unfactored operator, methods based on LU decompositions do not exhibit in three dimensions the known instability problem for the linear hyperbolic model equation. In ADI-type schemes the three-dimensional unfactored implicit operator is approximated by a product of three one-dimensional operators each of them being aligned with a specific coordinate direction. It is just the splitting of the implicit operator into three factors, however , which causes the mentioned instability for the delta-form version of the algorithm. Nevertheless ADI-type approximate factorization schemes can be made working well in three dimensions as was demonstrated by Pulliam and Steger [3,4] for Beam-Warming type schemes [5] . It was shown that conditional stability can be achieved by adding some artificial dissipation.

The development of an LU decomposition scheme is based on a somewhat different idea. Since the classical direct LU decomposition of the unfactored implicit operator is too expansive for multi-dimensional problems one has to resort to incomplete or approximate LU decompositon methods. In the latter concept a particular approximation to the unfactored implicit is chosen such that the desired LU representation directly will result. Hence for any dimensions only two factors appear which additionally possess the advantage to be easy invertible. Mostly this objective can be achieved by an appropriate lower order analogue of the original operator. Because for triangular matrices inversion is done in fact by simple forward and backward sweeps across the field these methods resemble the Symmetric Over-Relaxation (SSOR) approach.

Several approximate LU factorization schemes for hyperbolic equations have been proposed in the past. Steger [6] has pointed out the possibility of a relaxation LU-type solution of the inviscid conservation laws using his flux-split scheme. An interesting combination of an ADI-type scheme with an approximate LU scheme was presented by Obayashi and coworkers [7,8] .They inverted the one-dimensional ADI-factors by LU decomposition using a flux splitting concept.

In analyzing possible LU decompositions for hyperbolic equations Jameson and Turkel [9] found out that

well conditioned LU factors have to be diagonal dominant. Consequently a method was devised which enables each factor to be diagonal dominant. From that property stability of the factored block triangular system for any number of space dimensions was deduced. In the following a variant of the LU scheme, called LU-SSOR scheme was proposed by Jameson and Yoon [10]. It was concluded that in comparison to the LU implicit scheme the new LU-SSOR variant performs worse, also if combined with a multi grid method. Recently this conclusion was revised by the same authors[11,12]. Corresponding improvements of the scheme were rendered possible by abandoning time-marching and changing the scheme to an approximate Newton iteration approach operating on the steady state equations. On a variant of this scheme is reported in the course of this study.

Finally it should be mentioned that the scheme developed in [9] was applied by Buratynski and Caughey [13] to cascade flow problems.Subsequently an extension to three-dimensional turbomachinery flow problems was presented by Yokota and Caughey [14].

Quite recently a different approximate LU factorization scheme, proposed by Pan and Lomax [15], was applied to the Navier-Stokes equations. They use central-differencing for both implicit and explicit operators and tried to optimize the LU factors according to a linear analysis. Convergence could be improved by an explicit eigenvector annihilation procedure.

Governing Equations

The proper starting point for a finite-volume approach is the integra formulation of the steady state conservation laws

$$\int_S (\mathrm{A}\underline{v} + \mathrm{B})\cdot\underline{n}dS = 0. \qquad (1)$$

There S is the surface bounding a fixed volume in space, whereas A represents a certain property convected with the mass velocity $\underline{v}$ and B denotes a flux associated with A. If not noticed otherwise a bar below a quantity indicates a vector and a double bar a tensor or matrix.

From eq.(1) the specific conservation laws for mass,momentum and energy are recovered by substituting for A and B the following quantities

$$\begin{array}{lll} \text{continuity} & : & \mathrm{A} \equiv \rho \quad , \mathrm{B} \equiv 0 \\ \text{momentum} & : & \mathrm{A} \equiv \rho\underline{v} \quad , \mathrm{B} \equiv \underline{\underline{q}} \\ \text{energy} & : & \mathrm{A} \equiv \rho e_{tot} \quad , \mathrm{B} \equiv -\underline{\underline{q}}\cdot\underline{v} + \underline{q} \end{array} \qquad (2)$$

In usual notation ρ , $\underline{v}$, $\underline{q}$ are introduced as the mass density, the mass velocity vector and the heat flux vector, whereas $\underline{\underline{q}}$ denotes the stress tensor , and e the mass-specific internal energy. The mass-specific total energy e_{tot} is defined as $e_{tot} = e + 1/2(\underline{v}\cdot\underline{v})$.

To assure the general applicability of the numerical method the conservation laws have to be expressed in terms of a generalized curvilinear coordinate system $(x^1, x^2, x^3) \equiv (\xi, \eta, \zeta)$ which is related to the base cartesian coordinate frame $(x^{1'}, x^{2'}, x^{3'}) \equiv (x,y,z)$ by some mapping. The normal surface vector $\underline{n}dS$ of a surface element belonging to a coordinate surface $x^k = const.$ can be written as

$$d\underline{S}^k = \underline{n}^{(k)}\, dS^{(k)} = dS^k_{m'}\, \underline{g}^{m'}$$

where $dS^k_{m'}$ denotes the cartesian components of the normal surface vector and $\underline{g}^{m'}$ a cartesian base vector pointing into the direction $x^{m'}$. The components of the normal surface vector can be expressed in terms of transformation quantities via $dS^k_{m'} = \sqrt{g}\,\beta^k_{m'}$. There $\sqrt{g}$ defines the determinant of the jacobian of transformation $|\,\partial(x,y,z)/\partial(\xi,\eta,\zeta)\,|$ and $\beta^k_{m'}\,(\equiv \partial x^k/\partial x^{m'})$ denotes an element of the hybrid metric tensor. As an example the continuity equation can be written in terms of vector components as

$$\int_S \rho v^{n'}\, dS^k_{n'} = 0.$$

To get a direct finite-volume discretization for an elementary volume dV , bounded by successive surface elements dS^k_- and dS^k_+ belonging to the general coordinate surface x^k , the mean value theorem of integral calculus has to be applied , resulting in

$$\int_S \rho v^{n'}\, dS^k_{n'} = \sum_{k=1}^{3} \Delta_k[\overline{\rho v^{n'}}\,\delta S^k_{n'}] = 0 \qquad (3)$$

Here, for the moment, the delta operator should be understood as $\Delta_k[\bar{f}^{n'}\delta S^k_{n'}] = [\,\ldots\,]_+ - [\,\ldots\,]_-$. It is noted that the relation represents an exact equality and the order of the discretization error is determined by the definition of the mean value $\bar{f}^{n'}$ and by the accuracy in evaluating the components of the normal surface vector $\delta S^k_{n'}$.

The above procedure leading to a finite-volume discretization of the continuity equation can be repeated analogeously for the equations of momentum and energy. Dropping below the bars indicating a mean value one gets, after splitting the stress tensor in a viscous and a pressure contribution $\underline{\underline{q}} = -p\underline{\underline{I}} + \underline{\underline{\tau}}$, the following equations

$$\{\sum_{k=1}^{3} \Delta_k[(\rho v_{n'} v^{m'} + p\delta^{m'}_{n'} - C_1\tilde{\tau}^{m'}_{n'})\,\delta S^k_{m'}]\}\,\underline{g}^{n'} = 0 \qquad (4)$$

$$\sum_{k=1}^{3} \Delta_k[(\,\rho e_{tot} + p\,)v^{m'} - C_1\tilde{\tau}^{m'}_{n'}v^{n'} + q^{m'})\,\delta S^k_{m'}] = 0. \qquad (5)$$

The static pressure is denoted by p and the coefficient C_1 (= 1) will be redefined below in terms of similarity parameters if dimensionless quantities are introduced. The system of equations (3-5) is closed by assuming a perfect gas

$$p = (\kappa - 1)\,\rho e \qquad (6)$$

and the validity of Fourier's law of heat conduction.

$$q^{m'} = -C_2\, e_{i_3}\, \beta^{i}_{n'} g^{m'n'} \qquad (7)$$

Above C_2 is defined as the ratio λ / c_v, where λ denotes the coefficient of heat conduction and c_v the specific heat at constant volume. Further necessary relations are provided by assuming a Newtonian fluid.

$$\underline{\underline{g}} = (-p\delta^{m'}_{n'} + \tilde{\sigma}^{m'}_{n'})\, \underline{g}_{m'}\, \underline{g}^{n'} \qquad (8a)$$

$$\tilde{\sigma}^{m'}_{n'} = \frac{2}{3}\mu\, v^{s'}_{,r'}\, \beta^{r'}_{s'}\delta^{m'}_{n'} + \mu\,[v^{m'}_{,r'}\beta^{r'}_{n'} + (v_{n'})_{,r'}\beta^{r'}_{t}g^{tm'}] \qquad (8b)$$

Here the applied tensor notation indicates a partial derivative by a comma, e.g. $v^{m'}_{,r'} = \partial v^{m'}/\partial x^{r'}$. The temperature dependence of the dynamic viscosity μ is taken according to Sutherland's formula.

The equations (3) to (8b) can be converted to a dimensionless representation by defining

$$C_1 = \frac{\kappa^{1/2} Ma_\infty}{Re_L} \qquad C_2 = \frac{\kappa^{3/2} Ma_\infty}{Re_L\, Pr}\,(\frac{\tilde{\mu}}{\tilde{\mu}_\infty})$$

The similarity parameters introduced are the Mach number Ma_∞, the Reynolds number Re_L and the Prandtl number Pr.

$$\begin{aligned} Ma_\infty &\equiv \tilde{V}_\infty / \tilde{c}_\infty \\ Re_L &\equiv \tilde{V}_\infty \tilde{L} \,/\, (\tilde{\mu}_\infty / \tilde{\rho}_\infty) \\ Pr &\equiv c_{p\infty}\tilde{\mu}_\infty / \tilde{\lambda}_\infty \end{aligned}$$

There $\tilde{L}$ denotes a characteristic length, $\tilde{V}_\infty = (|\underline{v}\cdot\underline{v}|_\infty)^{1/2}$ the magnitude of freestream velocity, $\tilde{c}_\infty$ the speed of sound at infinity and $c_{p\infty}$ the specific heat at constant pressure.

The replacement of dependent and independent variables by their dimensionless counterparts would be consistent assuming the following relations. (To avoid any misunderstandings the quantities in their right dimensions are denoted for the moment by a tilde and conditions at infinity are indicated here and in the following by the subscript ∞).

$$\begin{aligned} x^{r'} &= \tilde{x}^{r'}/\tilde{L} & v^{r'} &= \tilde{v}^{r'}/(\tilde{c}_\infty/\sqrt{\kappa}) \\ \rho &= \tilde{\rho}/\tilde{\rho}_\infty & p &= \tilde{p}/\tilde{p}_\infty \\ T &= \tilde{T}/\tilde{T}_\infty & \mu &= \tilde{\mu}/\tilde{\mu}_\infty \\ q^{m'} &= \tilde{q}^{m'}/(\tilde{p}_\infty \tilde{c}_\infty/\sqrt{\kappa}) \end{aligned}$$

Numerical Method

For the numerical solution of the steady conservation laws the implicit LU-SSOR scheme [11,12] is adopted. Some key features of the method together with some further developments are presented below.

For the approximate solution of the steady state conservation laws (3-5) a second-order cell-centered finite-volume scheme is applied. Such a scheme is derived by defining the fluxes at the cell faces from simple algebraic mean values of the conserved variables, which are assumed to be placed at the cell centers. The vector of conserved variables $\underline{q}$ (which should not be confused with the heat flux vector introduced above) is defined as

$$\underline{q} = (\rho\,,\, \rho v^{1'}\,,\, \rho v^{2'}\,,\, \rho v^{3'}\,,\, \rho e_{tot})^T$$

The numerical method is most easily presented in symbolic form.
Defining the discrete residual of (3-5) resulting from a finite-volume discretization as

$$\begin{aligned} \underline{R} = \quad & \Delta_1 (\underline{E} - \underline{E}_v - \underline{E}_D) + \Delta_2 (\underline{F} - \underline{F}_v - \underline{F}_D) \\ & + \Delta_3 (\underline{G} - \underline{G}_v - \underline{G}_D) \end{aligned} \qquad (9)$$

where $\underline{E}, \underline{F}, \underline{G}$ and E_v, F_v, G_v represent the inviscid and viscous flux vectors into the general coordinate directions x^1, x^2 and x^3, respectively. For control of nonlinear instabilities any central differenced scheme has to be provided by suitable dissipation operators which are indicated by lower indices D .
Then a Newton-iteration would read

$$(\frac{\partial \underline{R}}{\partial \underline{q}})^n\, \delta\underline{q}^n + \underline{R}^n = 0. \qquad (10)$$

Here the upper index indicates the iteration count and $\delta\underline{q}^n$ is defined as $\delta\underline{q}^n = \underline{q}^{n+1} - \underline{q}^n$. In general the computation and inversion of of the functional matrix $\partial\underline{R}/\partial\underline{q}$ is too costly, so that an approximate form has to be found such that the inversion is easy and stable. A choice which has been found beneficial [9] resembles that of flux-vector splitting. Because the particular construction only affects the implicit operator a rather crude choice fulfills the requirements for diagonal dominance of the coefficient matrices.

For definition of the functional matrix some jacobians of the different flux vectors are needed.

$$\underline{\underline{A}} \equiv \frac{\partial \underline{E}}{\partial \underline{q}} \qquad \underline{\underline{A}}_v \equiv \frac{\partial \underline{E}_v}{\partial \underline{q}} \qquad \underline{\underline{A}}_D \equiv \frac{\partial \underline{E}_D}{\partial \underline{q}}$$

$$\underline{\underline{B}} \equiv \frac{\partial \underline{F}}{\partial \underline{q}} \qquad \underline{\underline{B}}_v \equiv \frac{\partial \underline{F}_v}{\partial \underline{q}} \qquad \underline{\underline{B}}_D \equiv \frac{\partial \underline{F}_D}{\partial \underline{q}}$$

$$\underline{\underline{C}} \equiv \frac{\partial \underline{G}}{\partial \underline{q}} \qquad \underline{\underline{C}}_v \equiv \frac{\partial \underline{G}_v}{\partial \underline{q}} \qquad \underline{\underline{C}}_D \equiv \frac{\partial \underline{G}_D}{\partial \underline{q}}$$

Then an appropriate approximation to the functional matrix in eq.(10) could be

$$(\frac{\partial \tilde{\underline{R}}}{\partial \underline{q}}) = D_\xi\, \underline{\underline{A}} + D_\eta\, \underline{\underline{B}} + D_\zeta\, \underline{\underline{C}}. \qquad (11)$$

The experience shows that in principle only the inviscid flux jacobians have to be considered for definition of the implicit operator, also for viscous calculations. Although robustness and stability may be improved for severe problems by including into the implicit operator an approximation to the artificial dissipation operator and by parts the physical viscous flux jacobians , for a further discussion the basic scheme (11) is sufficient.

The difference operators D_ξ etc. are written as a sum of first order forward (Δ_ξ) and backward (∇_ξ) difference operators.

$$D_\xi \underline{A} = \Delta_\xi \underline{A}^- + \nabla_\xi \underline{A}^+ \tag{12}$$

Now the particular flux jacobians $\underline{A}^+$ and $\underline{A}^-$ etc. are defined in such a way that they possess only non-negative and non-positive eigenvalues

$$\underline{A}^\pm = \frac{1}{2}(\underline{A} \pm r_A \underline{I}) \tag{13a}$$

$$r_A \geq \max(|\lambda_A|) \tag{13b}$$

That is achieved by defining r_A as a value which has to be equal or greater than the spectral radius of $\underline{A}$

By sweeping forward and backward through the field the resulting relations can be combined similar to a SSOR method [12] and it turns out that the implicit operator in eq.(11) can be approximately factorized into a product of a *strictly lower triangular matrix* $\underline{L}$, *a diagonal matrix* $\underline{D}$ and an upper triangular matrix $\underline{U}$. Hence the basic scheme can be written as

$$(\underline{L}\,\underline{D}^{-1}\,\underline{U})\,\delta\underline{q}^n = -\underline{R}^n \tag{14}$$

with

$$\begin{aligned}\underline{L} &= \nabla_\xi \underline{A}^+ + \nabla_\eta \underline{B}^+ + \nabla_\zeta \underline{C}^+ - \underline{A}^- - \underline{B}^- - \underline{C}^- \\ \underline{D} &= (r_A + r_B + r_C)\,\underline{I} \\ \underline{U} &= \Delta_\xi \underline{A}^- + \Delta_\eta \underline{B}^- + \Delta_\zeta \underline{C}^- + \underline{A}^+ + \underline{B}^+ + \underline{C}^+\end{aligned} \tag{15}$$

Now stability should be enhanced providing diagonal dominance for each factor [9]. Consider as an example the L-factor for which rearrangement will allow to write :

$$\begin{aligned}\underline{L} = (r_A + r_B + r_C)\,\underline{I}_{i,j,k} &- \tfrac{1}{2}(\underline{A} + r_A \underline{I})_{i-1,j,k} \\ &- \tfrac{1}{2}(\underline{B} + r_B \underline{I})_{i,j-1,k} \\ &- \tfrac{1}{2}(\underline{C} + r_C \underline{I})_{i,j,k-1}\end{aligned}$$

It is evident that diagonal dominance is only assured if the quantities $r_{A\,i,j,k}$ and $r_{A\,i-1,j,k}$ etc. are redefined such that they are equal and simultaneously the maximum of both original values defined after eq.(13b). That is

$$r_A^- = \max(r_{A\,i,j,k}, r_{A\,i-1,j,k})_{orig}$$

$$r_{A\,i,j,k} := r_A^-$$

$$r_{A\,i-1,j,k} := r_A^-$$

Corresponding settings following for the U-factor suggest also a modified diagonal matrix D.

$$\underline{D} = \tfrac{1}{2}(r_A^- + r_A^+ + r_B^- + r_B^+ + r_C^- + r_C^+)\,\underline{I}$$

In fact inversion of the scheme (14) is accomplished by sweeping along diagonal planes I+J+K = const. across the domain. Then during the inversion process all variables needed from the off-diagonals are already updated, allowing a variation of the straightforward procedure. In inverting the modified L-factor we obtain from (14):

$$\begin{aligned}(r_A + r_B + r_C)\,\underline{I}_{i,j,k}\,\delta\bar{\underline{q}}_{i,j,k} = -\underline{R}^n &+ \underline{A}^+_{i-1,j,k}\,\delta\bar{\underline{q}}_{i-1,j,k} \\ &+ \underline{B}^+_{i,j-1,k}\,\delta\bar{\underline{q}}_{i,j-1,k} \\ &+ \underline{C}^+_{i,j,k-1}\,\delta\bar{\underline{q}}_{i,j,k-1}\end{aligned}$$

To avoid the explicit evaluation of jacobian matrices the intermediate flux states can be approximated by a Taylor series expansion

$$\bar{\underline{E}}^+ = (\underline{E}^+)^n + \frac{\partial \underline{E}^+}{\partial \underline{q}}(\bar{\underline{q}} - \underline{q}^n) + O(|\delta\bar{\underline{q}}|^2)$$

$$\delta\bar{\underline{E}}^+ = \bar{\underline{E}}^+ - \underline{E}^{+n} = \underline{A}^+ \delta\bar{\underline{q}} + O(|\delta\bar{\underline{q}}|^2)$$

Now the scheme (14) is inverted by the following steps :

$$\begin{aligned}\delta\bar{\underline{q}}_{i,j,k} &= -\underline{R}^n_{i,j,k} + \delta\bar{\underline{E}}^+_{i-1,j,k} + \delta\bar{\underline{F}}^+_{i,j-1,k} + \delta\bar{\underline{G}}^+_{i,j,k-1} \\ \delta\bar{\underline{q}}_{i,j,k} &= \underline{D}^{-1}_{i,j,k}\,\delta\bar{\underline{q}}_{i,j,k} \\ \delta\underline{q}^n_{i,j,k} &= \underline{D}^{-1}_{i,j,k}(\delta\bar{\underline{q}}_{i,j,k} - \delta\underline{E}_{i+1,j,k} - \delta\underline{E}_{i,j+1,k} - \delta\underline{G}_{i,j,k+1})\end{aligned} \tag{16}$$

where

$$\delta\bar{\underline{E}}^\pm = \underline{E}^\pm(\bar{\underline{q}}) - \underline{E}^\pm(\underline{q}^n)$$

$$\delta\underline{E}^\pm = \underline{E}^\pm(\bar{\underline{q}}) - \underline{E}^\pm(\underline{q}^n)$$

In comparison to the straightforward inversion of scheme (14) no degradation in performance was observed with the cost-effective relaxation-type inversion (16).

Artificial Dissipation Model

As mentioned previously including physical viscous and artificial dissipative operators implicitly will support the stability of the scheme in some cases.

The explicitly added dissipation fluxes $\underline{E}_D$ *etc. are* defined as a combination of first and third order operators, a construction introduced by Jameson et al [1]. This particular adaptive dissipation model proved to produce solutions of flows with discontinuities without oscillations. In *principle the dissipation flux has the form*

$$\underline{E}_D = S(\epsilon^{(2)} + \epsilon^{(4)} \Delta_\xi \nabla_\xi)\delta_\xi \underline{q}$$

where δ_ξ is a central difference operator and $\epsilon^{(2)}$ and $\epsilon^{(4)}$ *are adaptive coefficients. The scaling factor S is chosen to* be proportional to the spectral radius of the corresponding inviscid flux jacobians. The coefficient $\epsilon^{(4)}$ of the third order operator provides background dissipation for smooth regions of the flow and will be switched off in the vicinity *of shocks, which are essentially captured by a pressure* sensor included in the definition of the coefficient $\epsilon^{(2)}$.

$$\epsilon^{(2)}_{i+1/2} = k^{(2)} \max(\nu_{i+1}, \nu_i)$$

$$\epsilon^{(4)}_{i+1/2} = \max(0, (k^{(4)} - \epsilon^{(2)}_{i+1/2}))$$

$$\nu_i = \frac{\Delta_\xi \nabla_\xi p}{(4 + \Delta_\xi \nabla_\xi) p}$$

As will be shown later the sensor ν should be modified at shock waves where the pressure jump is no more O(1).

Implicit Dissipation Operator

In order to restrict the implicit dissipation operator to at most second order the jacobian $\underline{A}_D$ is simply approximated by

$$\underline{A}^i_D = a_1 S(\epsilon^{(2)} + a_2 \epsilon^{(4)}) \underline{I}$$

resulting into the implicit representation

$$D_\xi \underline{E}^i = \delta_\xi \underline{A}^i_D \delta_\xi \underline{q} = [E^{1/2}_\xi (\underline{A}^i_D \delta_\xi) - E^{-1/2}_\xi (\underline{A}^i_D \delta_\xi)] \underline{q}$$

Here the quantities a_1 and a_2 are adjustable coeficients and $E^{\pm 1/2}_\xi$ etc. denote a shifting operator whereby the superscript defines the index shift and the subscript the corresponding direction. Because the implicit dissipation flux jacobians $\underline{A}^i_D$ etc. have diagonal form they do not affect the overall definition of the LU factors (15) and therefore corresponding modifications are smoothly fitted into the algorithm. It is noted that inclusion of the implicit dissipation operator will maintain diagonal dominance for each factor.

Obviously the particular construction of smoothing operators will influence the performance of each central differenced scheme. Variations and alternatives were discussed recently by Swanson and Turkel [16], while Pulliam [17] pointed out the connections and the equivalence of an upwind scheme with a central difference scheme enhanced by an appropriate dissipation model.

Implicit Viscous Operator

For Navier-Stokes calculations the implicit factors is enhanced by a thin-layer approximation for the viscous fluxes in an attempt to reduce the operation count.

Assuming the ζ – direction emanating from the body the corresponding thin-layer viscous flux $\underline{G}^{TL}_v$ and its jacobian $\underline{C}^{TL}_v$ will only have derivatives in that direction. However a direct implementation will not preserve diagonal dominance to the implicit LU factors. Therefore an operator is chosen similar to that developed above approximating the dissipation flux. In principle the change of the viscous flux vector $\delta \underline{G}^{TL}_v = (\underline{G}^{TL}_v)^{new} - (\underline{G}^{TL}_v)^{old}$ can be represented as

$$\delta \underline{G}^{TL}_v = \underline{C}^{TL}_v \delta \underline{q} \qquad (:= \underline{a} \frac{\partial}{\partial \zeta} [\frac{\partial \underline{\beta}}{\partial \underline{q}} \delta \underline{q}])$$

To get an appropriate jacobian it is assumed that the functional $\partial \underline{\beta} / \partial \underline{q}$ is independent of position, which produces a balanced operator.

$$\delta \underline{G}^{TL\times}_v = \underline{C}^{TL\times}_v \delta_\xi (\delta \underline{q}) \qquad (:= \underline{a} \frac{\partial \underline{\beta}}{\partial \underline{q}} \frac{\partial}{\partial \zeta} \delta \underline{q})$$

and therefore we get

$$D_\xi (\delta \underline{G}^{TL\times}_v) = \delta_\xi \underline{C}^{TL\times}_v \delta_\xi (\delta \underline{q}).$$

However the simplified jacobian $\underline{C}^{TL\times}_v$ has not diagonal form as was the case for the corresponding dissipation jacobians $\underline{A}^i_D$. Concerning the additional arithmetic operations involved for inverting the 5x5 block matrices , that situation - although working fine - ist not optimal. Therfore future developments will be directed on possibilities for replacing the functional matrix by a suitable diagonal approximation.

Boundary Conditions

Finally some remarks concerning the treatment of implicit and explicit boundary conditions.

For problems with subsonic in- or outflow far field boundaries conditions resulting from the locally one-dimensional Riemann invariants are applied explicitly. This treatment has proven to damp out disturbances reflecting at the outer boundary. For supersonic conditons at inflow boundaries corresponding free stream values are fixed whereas at outflow boundaries a consistent first order extrapolation to all dependent variables is used. At the body the pressure is obtained by an approximation to the normal momentum equation. For viscous calculations the viscous contribution is neglected resulting into $\partial p / \partial n \equiv 0$, which should be a sufficient conditon for high speed flows.

On the implicit side for all convection terms the change in the dependent variables of the fictious boundary cells is assumed to be zero, which is equivalent to a Dirichlet boundary condition. For the implicit dissipation operator and the corresponding viscous thin-layer operator a zero flux conditon is implemented. Concerning the dissipation terms this treatment is also consistent with those boundary conditions required for the explicit side.

Results

A desirable feature of the numerical method developed in the last section would be the support from a multi grid method. Although the code can run in a multi grid mode all results presented are obtained by single grid computations. Up till now no serious effort was directed to the question how the LU factors have to be modified to get good multi grid smoothing performance. However the feature of prolongating the current solution to the next finer mesh was utilized to get an appropriate initial guess on the final mesh system.

In addition by input option the code can be forced to work with the inviscid or viscous equation set. In the case of the Navier-Stokes equations the laminar or turbulent flow option may be chosen and the order of approximation of the viscous stress tensor can be specified . In this respect the thin-layer, the full thin-layer and the full viscous approximation of the Navier-Stokes equations are available. The turbulent flow modelling is based on the purely algebraic turbulence model of Baldwin and Lomax [18].

With the method developed some flow problems have been investigated belonging to quite different speed regimes. As the first example a viscous flow simulation past a sphere at low Mach numbers is presented.

Sphere Flow

It is well known that besides the simple geometrical shape of a sphere the flow around such a geometry has a complex structure which depends heavily on the Reynolds-number as the important viscous similarity parameter.

For various values of the Reynolds-number the flow around a sphere can be classified into four regimes (Fig. 1), where the decision upon the corresponding range is made according to the behaviour of the drag coefficient as function of the Reynolds-number [19]. In the subcritical regime the drag is nearly independent of Reynolds-number and extends up to $Re_D \lesssim 3 \cdot 10^5$, where the Reynolds-number is based on the diameter of the sphere. The critical regime is characterized by a sharp drop of the drag coefficient reaching a minimum at $Re_D \lesssim 3 \cdot 10^5$which serves as the distinguished point separating the critical from the supercritical regime. With increasing Reynolds-number ($Re_D \gtrsim 3.7 \cdot 10^5$) also the drag coefficient increases slowly in the supercritical regime reaching an almost asymptotic state, taken as a critera for the beginning of the transcritical range. It is clear that this observed behaviour can be directly correlated with the properties of laminar and turbulent flow and the phenomena of transition from the laminar to the full turbulent state.

Two flow cases are considered in detail. According to the experiments studies of Achenbach [19] the chosen subcritical case is a purely laminar flow with a Reynolds-number of $1.62 \cdot 10^5$, whilst the transcritical case considered ($Re_D = 5 \cdot 10^6$) is found to be a mostly turbulent flow where natural transition from laminar to turbulent flow behaviour is observed approximately at $\phi \cong 60°$.

For the laminar flow ($Re_D = 1.62 \cdot 10^5$) considered a spherical grid system of 65 x 65 x 49 nodes was applied, where the mesh system in radial direction consisted of 49 points with a resolution for the first cells adjacent to the sphere surface $\Delta \simeq 7 \cdot 10^{-5}$ This is based on a definition of the sphere diameter D = 1. The outer boundary is placed 15 diameters away from the sphere.

The grid system generated for the transcritical case consisted of 65 points in radial direction with a minimum grid spacing at the sphere surface of $\Delta = 5 \cdot 10^{-6}$ and an outer boundary placed 12.5 diameters away from the sphere. Both surface meshes were identical and defined to be equally spaced by 64 x 64 intervals.

For both flow cases a lateral symmetry condition was assumed in an attempt to reduce the computational costs without restricting too much the flow physics simulated.

Laminar Flow Results: The laminar flow simulation is based on the parameters $Re_D = 1.62 \cdot 10^5$ and $Ma = 0.3$. After 500 iterations on the finest grid the L_1 norm of continuity equation was reduced by more than 3 decades . On a fairly low error level ($L_2 \cong 5 \cdot 10^{-7}$) no further convergence was obtained. A closer look on the results during some stages of the iteration process showed a clearly unsteady wake behaviour which agrees qualitatively with the experimental findings. In an investigation on the wake structure of flows past spheres Taneda [20] reports on a progressive wave motion of the sphere wake for the range $10^4 \lesssim Re_D \lesssim 3.8 \cdot 10^5$. The wave can be described by a plane containing the streamwise axis through the centre of the sphere. Thereby the plane rotates slowly and irregularly about that axis. At Reynolds-numbers ranging from $3.8 \cdot 10^5$ to 10^6 the sphere wake formes a pair of streamwise line vortices at a short distance from the streamwise axis. Also this vortex pair rotates slowly and randomly about that axis. In all ranges mentioned the sphere wake is not axisymmetric. To illustrate somewhat the complex wake flow a sketch of the vortex structure in the range $3.8 \cdot 10^5 \lesssim Re_D \lesssim 10^6$ (after [20]) is shown in Fig. 2.

So it turns out that the flow structure also for laminar flow is highly complex. Therefore the numerical simulation of such a flow requires a high spatial resolution of the solution domain and simultaneously a high time accuracy to resolve adequately all existing flow scales and modes. The method used for the present simulations is based on an approach neglecting the correct time scales. Therefore from the results only the resolution of the main features of the flow can be expected.

Fig. 3a-c show for three different iteration stages the pressure distribution around the sphere in the symmetry plane. From the figures it is obvious that severe separation processes are taking place on the rear side, indicating a sweeping motion of the wake flow. The influence on the stagnation region is apparently weak.

A better understanding of the flow structure for the depicted solution states is depicted in Fig. 4 by corresponding velocity vector fields. The strongly changing velocity fields show no well established recirculation bubbles at the rear side but a confuse structure with at least two stagnation points on the back which may be an indication for leaving line vortices.

A comparison between experiments and theory in terms of the wall pressure distribution around a sphere is presented in Fig. 5. Because of the asymmetric flow structure on the rear side we have depicted the spread of the results in that region by inserting the extrema at destinct circumferential angle ϕ. The figure shows clearly that the computational results fluctuate around the measurements of Achenbach [19].

What effect the wake flow structure has on wall stress vectors at the rear side is illustrated in Fig. 6. There the wall stress vectors are shown on the lefthand-side and the direction of these vectors alone on the righthand-side. From this picture complex systems of separation lines can easily be detected giving an impression of the random behaviour of the flow in that region.

The comparison to the experimental skin-friction results of Achenbach is made in Fig. 7. In order to provide a meaningful comparison the representation of the theoretical results is restricted to the data along the meridians of the symmetry plane. This choice is easily explained by the complex pattern of the wall stress vectors seen in Fig.6.

It can be stated that in the attached flow region the agreement is rather good, if one remembers that the experimental data are obtained by an indirect method which is calibrated by a well known method of laminar boundary layer theory [19].

Turbulent Flow Results: The case considered is described by the parameters $Re_D = 5 \cdot 10^6$ and $Ma = 0.1$. Laminar to turbulent transition was fixed at $\phi = 60°$.

According to the presentation of laminar results the corresponding turbulent pressure distribution in the symmetry plane is depicted in Fig. 8. It is recognized that the structure is much more organized and up to $\phi < 120°$ nearly axisymmetric. Comparison of experimental and theoretical wall pressure data is made in Fig. 9. The theoretical results are concentrated in a more narrow band

indicating a nearly axisymmetric behaviour. However, the pressure level on the rear side is predicted too high.

Looking on the velocity vector field (Fig. 10), an almost perfect vortex loop appears. Up to now it is an open question, if the solution with continuing iterations will become similar random as in the laminar case. However, the experiments of Taneda [20] indicate a well organized and more steady wake flow for high Reynolds-numbers - an observation also available from the numerical simulation.

In Fig. 11 the skin friction results are depicted, showing an agreement qualitative in nature between experiments and simulation. Although the transition from laminar to turbulent flow was fixed at $\phi = 60°$ a strong upstream effect resulted. Also the separation at the rear side is predicted too late compared to the experimental data. Up to now no serious investigations were conducted to study the sensitivity of the skin friction peak-level on the position of the transition point. In accordance to the skin friction data the wall stress vectors for the turbulent case show a nearly axisymmetric behaviour (Fig. 12).

Hemisphere-Cylinder Flow

An interesting three-dimensional problem belonging to the transonic speed range is the flow around a hemisphere cylinder at incidence. Quite recently extensive theoretical studies facing this problem were conducted by Ying et al [21,22]. In the earlier work [21] the problem was considered mainly for $Ma = 1.2$ for various angles of attack $0 \leq \alpha \leq 19°$ and compared with available experimental data [23,24]. It turned out that these laminar flows exhibit a broad variety of separation phenomena and associated topological structures which was the reason to reinvestigate the particular case $Ma = 1.2, \alpha = 19°$ in a more detailed manner [22]. In that study successively finer grids were used to identify convergence of flow pattern. Interestingly flow topology changed with grid refinement and became asymmetric in the finest mesh used (101x100x81 points).

Also in the present study the particular laminar flow case ($Ma = 1.2$, $Re_D = 4.45 \cdot 10^5$, $\alpha = 19°$) served as an additional test case. The spherical type coordinate system used consisted of 49 points in the streamwise direction, 25 points in the circumferential direction for the half plane and 49 points normal to the body.

In Fig.13 and Fig.14 the static pressure and Mach number distribution is shown together with an enlarged map of the nose region. It is recognized that the bow and leeside shock wave is well captured . From the highly structured Mach number field on the leeside just behind the sphere-cylinder junction it can be deduced that a complex interacting flow field has established. Although not shown here, despite the relatively coarse mesh system the experimentally observed owl eyes and the primary and secondary separation lines were well captured in the simulation.

In Fig. 15 the streamwise wall pressure distributions on the leeside and the 90° -line are depicted. The present results are close to those of Ying et al [21] for the leeside, however show some remarkable differences on the 90° -line. There the results of Ying et al deviate substantially from the data of both experiments. The reasons for these deviations are not clear, because the results of [21] are based on a slightly more refined mesh.

It is mentioned that the above results were obtained in 300 iterations and a error norm reduction of the residuals of continuity equation of almost 3 decades.

Hypersonic Flow Past a Reentry Vehicle

The last example presented is the hypersonic flow past a complete reeentry vehicle. At the same free stream conditions ($Ma = 8$, $\alpha = 30°$) a viscous and an inviscid calculation was performed in order to identify the effect of viscosity on the overall flowfield. For both computations the fluid was assumed to behave as a perfect gas. Additionally, in the viscous case a laminar flow opposed to an adiabatic vehicle wall was assumed.

The task of computing the flow around a complete complex vehicle is not trivial and begins with the challenge of generating an appropriate mesh system. For the geometry at hand which is one of the proposed designs for the european HERMES space shuttle it appeared advantageously to adopt a one-block wrapped-around coordinate system. Such a coordinate system is of spherical type at the nose and therefore possesses a singular line emanating from the very nose. However also at the nose extreme conditions caused by the bow shock have to be expected, so that the singular line problem has to be treated carefully. Moreover in hypersonic flow past blunt bodies at high incidence the shock layer at the windward side becomes thin whereas at the leeward side the bow shock gets far away. Therefore it is desirable to have a coordinate system which approximately follows the outermost shock wave in an attempt to waste only a small fraction of mesh points available. Clearly this fact pays only for schemes as the present one which are capturing all shocks in the solution domain. Besides this point of view the underlying coordinate system should be - at least in regions adjacent to walls - approximately orthogonal to prevent large discretization error effects. Also the mesh should allow to be applied for space marching computations. For that purpose the mesh system should be constructed of planar cross sections. To meet all these requirements various grid generation techniques have been combined.

At the nose an spherical-type mesh system was generated using an algebraic approach. In front of the cockpit the mesh was forced to be planar in cross sections x = const. for over the remaining part of the vehicle. There a hyperbolic mesh generation procedure was applied. However in the hyperbolic approach, where the mesh is generated by marching outwards from the body, no control is given to meet an outer specified shape. Therefore the hyperbolic mesh was marched beyond the specified boundary and then the grid points were redistributed along the coordinate direction normal to the body. Distortions generated by this procedure were smoothed out by an elliptic mesh generation method. Hence in regions nearby the vehicle the mesh is expected to be approximately orthogonal and simultaneously the mesh is within a specified outer contour.
Such an approach is very time consuming and could only be accomplished in collaboration with Stephan Leicher at Dornier company. A more detailed description together with hypersonic flow results will be given in a forthcoming paper.

Fig. 16 shows the surface mesh around HERMES vehicle generated by the procedure described above. The grid system consists of 97 points in axial and 129 points in circumferential direction for the half vehicle. It is noted that the mesh at the nose singular point is made equidistant in the circumferential direction in order to facilitate the treatment at the singular line. Also at wing leading edges and at the wing-winglet junction the grid is refined accordingly. Fig. 17 depicts the strucure of the surface mesh

at the bottom and the top side. The generated coordinate system (129 points in circumferential and 65 points in normal direction) for an Euler computation in different cross sections is shown in Fig. 18. It is recognized that the mesh system follows the expected bow shock.

Fig. 19 depicts the Mach number and pressure distribution in the symmetry plane together with a detailed map of the nose region. The solutions presented show the bow and the canopy shock wave properly resolved, and any perturbations originating from the geometric singularity at the nose tip are almost not visible.

Before entering the discussion and comparison of inviscid and viscous computations some remarks concerning convergence of the solutions. For the inviscid case the residual error reduction measured by the drop of the L_2 norm was 3 orders of magnitude in the finest mesh, achieved in 350 iterations. For the viscous computation only 200 iterations were possible in the moment of writing and therefore the results (although the corresponding residual norm was reduced by 2 decades) should be looked as preliminary in nature.

In Fig. 20 for a distinct cross section (x = 7.8m) viscous and inviscid results are compared. Fig. 20a and Fig. 20b show the Mach number distribution for viscous and inviscid flow. Obviously the solution in the outer part of the shock layer is almost identical but show remarkable differences in the vicinity of the vehicle. Whereas the inviscid simulation depicts a cross flow shock wave above the wing and above the cargo bay corresponding effects are strongly smoothed in viscous flow. Also the development of vortex separation over the cargo bay is noted.

The mentioned effects are more pronounced at a station downstream (Fig. 21). Here Mach number distributions are compared in a cross section containing the upward directed wing panel, named from now on as winglet. Additionally to the cross flow phenomana observed in Fig. 20, at x = 12.7 the flow field exhibits a shock wave at the winglet leading edges. Also the cross flow shock above the wing is now first aligned diagonal to the vertical fuselage wall and than experiences a deviation of approximately 90 degree. This topology is known from supersonic corner flows where the lower shock front is observed to be parallel to the flat plate. A closer look on the results (Fig. 22) reveals the unrealistic prediction of the inviscid simulation. Fig. 22c shows above the wing a Mach number in the order of 15 which occurs simultaneously with very low pressure and density values.

In this respect much more realistic appears the viscous flow behaviour (Fig. 22a,b). There the maximum Mach number is shown to be in the order of the free stream value. Also jet tongues known from corner flow studies seem to be captured. More extreme flow conditions are expected to exist in the end cross sections, presented in Fig. 23 and Fig. 24.

In Fig. 25 the direction of wall stress vectors on the HERMES vehicle are presented as a preliminary result. Obviously shock induced separation occurs above the wing, above the cargo bay and in front of the cockpit as a result of the canopy shock. Separation induced by corner flow particularities may exist.

However these various flow phenomena have to be analyzed carefully in great detail in order to draw conclusions being valuable for future design development.

Conclusions

An improved LU scheme for solution of three-dimensional Euler and Navier-Stokes equations has been presented.

The robustness achieved was demonstrated by the ability of treating flow problems of quite different velocity scales without any major changes to the method. It was shown that the numerical results obtained are in reasonable to close agreement to the experimental data available. The hypersonic flow simulation results look reliable and further development of the method to include real gas conditions are in progress.

From the numerical point of view it appears highly desirable to combine efficiently the LU scheme with a multi grid method. However,as a side condition such a scheme has to work also for complex problems at hypersonic speeds.

References

[1] Jameson, A. ; Schmidt, W. and Turkel, E.
Numerical Solutions of the Euler Equations by Finite Volume Methods Using Runge-Kutta Time Stepping Schemes
AIAA-81-1259 , 1981

[2] Jameson, A.
Transonic Flow Calculations for Aircraft
Lecture Notes in Mathematics, Vol. 1127 ,
Numerical Methods in Fluid Dynamics, edited by F.Brezzi, Springer-Verlag, 1985 , pp. 156-242

[3] Pulliam, T. H. and Steger, J. L.
Implicit Finite Difference Simulations of Three-Dimensional Compressible Flow
AIAA Journal, Vol.18, 1980, pp.159-167

[4] Pulliam, T. H. and Steger, J. L.
Recent Improvements in Efficiency, Accuracy and Convergence for Implicit Approximate Factorization Algorithms
AIAA-85-0360 , 1985

[5] Beam, R. and Warming, R. F.
An Implicit Finite-Difference Algorithm for Hyperbolic Systems in Conservation-Law-Form
J. Comp. Phys., Vol.22, 1976, pp.87-110

[6] Steger, J. L.
A Preliminary Study of Relaxation Methods for the Inviscid Conservative Gasdynamics Equations Using Flux Splitting
NASA-CR-3415 , March 1981

[7] Obayashi S. and Kuwahara, K.
LU Factorization of an Implicit Scheme for the Compressible Navier-Stokes Equations
AIAA-84-1670, 1984

[8] Obayashi S. and Fujii, K.
Computation of Three- Dimensional Viscous Transonic Flows with the LU Factored Scheme
AIAA-85-1510, 1985

[9] Jameson, A. and Turkel, E.

Implicit Schemes and LU-Decompositions
Math. Comp.,Vol. 37, 1981 , pp.385-397

[10] Jameson, A. and Yoon, S.
LU-Implicit Schemes with Multiple Grids for the Euler Equations
AIAA-86-0105 , 1986

[11] Yoon, S. and Jameson, A.
A Multigrid LU-SSOR Scheme for Approximate Newton-Iteration Applied to the Euler Equations
NASA-CR-17954, 1986

[12] Yoon, S. and Jameson, A.
An LU-SSOR Scheme for the Euler and Navier-Stokes Equations
AIAA-87-0600 , 1987

[13] Buratynski, E.K. and Caughey, D.A.
An Implicit Lu Scheme for the Euler Equations Applied to Arbitrary Cascades
AIAA-Journal, Vol. 24, 1986, pp.39-46

[14] Yokota, J.W. and Caughey, D.A.
An LU Implicit Multigrid Algorithm For the Three-Dimensional Euler Equations
AIAA-87-0453,1987

[15] Pan, D. and Lomax, H.
A New Approximate LU Factorization Scheme For the Reynolds-Averaged Navier-Stokes Equations
AIAA-86-0337,1986

[16] Swanson, R.C. and Turkel, E.
Artificial Dissipation and Central Difference Schemes For the Euler and Navier-Stokes Equations
AIAA-87-1107,1987

[17] Pulliam, T.H.
Artificial Dissipation Models For the Euler Equations
AIAA-85-0437,1985

[18] Baldwin, B.S. and Lomax, H.
Thin-Layer Approximation and Algebraic Model For Separated Turbulent Flows
AIAA-78-0257, 1978

[19] Achenbach, E.
Experiments on the Flow Past Spheres at Very High Reynolds Numbers
J. Fluid Mech., Vol.54, 1972, pp. 565-575

[20] Taneda, S.
Visual Observations of the Flow Past a Sphere at Reynolds Numbers Between 10^4 and 10^6
J. Fluid Mech., Vol.85, 1978, pp. 187-192

[21] Ying, S.X.; Steger, J.L.; Schiff, L.B.; Baganoff, D.
Numerical Simulation of Unsteady , Viscous, High-Angle-Of-Attack Flows Using a Partially Flux-Split Algorithm
AIAA-86-2179, 1986

[22] Ying, S.X.; Schiff, L.B.; Steger, J.L.
A Numerical Study of the Three-Dimensional Separated Flow Past a Hemisphere Cylinder
AIAA-87-1207, 1987

[23] Hsieh, T.
An Investigation of Seperated Flows about a Hemisphere-Cylinder at Incidence in the Mach Number Range from 0.6 to 1.5
AIAA-77-0179, 1977

[24] Lim, T.T. and Meade, A.J.
Surface Pressure and Oil-Flow Measurements on a Hemisphere-Cylinder at Incidence in Transonic Flow
NASA TM in preparation, 1987 (as cited in Ref.22)

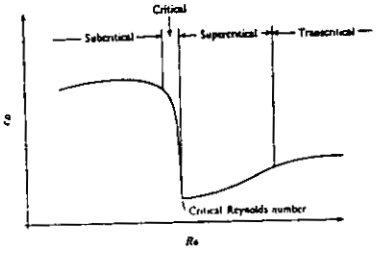

Fig. 1 : Flow regimes of the flow around a sphere (after [19])

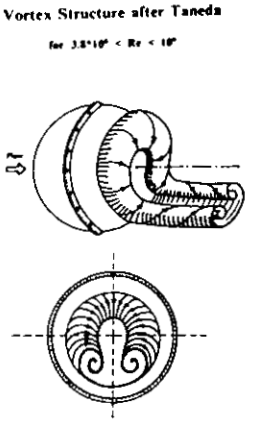

Fig. 2 : Vortex structure of sphere wake flow in the range $3.8 \cdot 10^5 \leq Re_D \leq 10^6$ after Taneda [20]

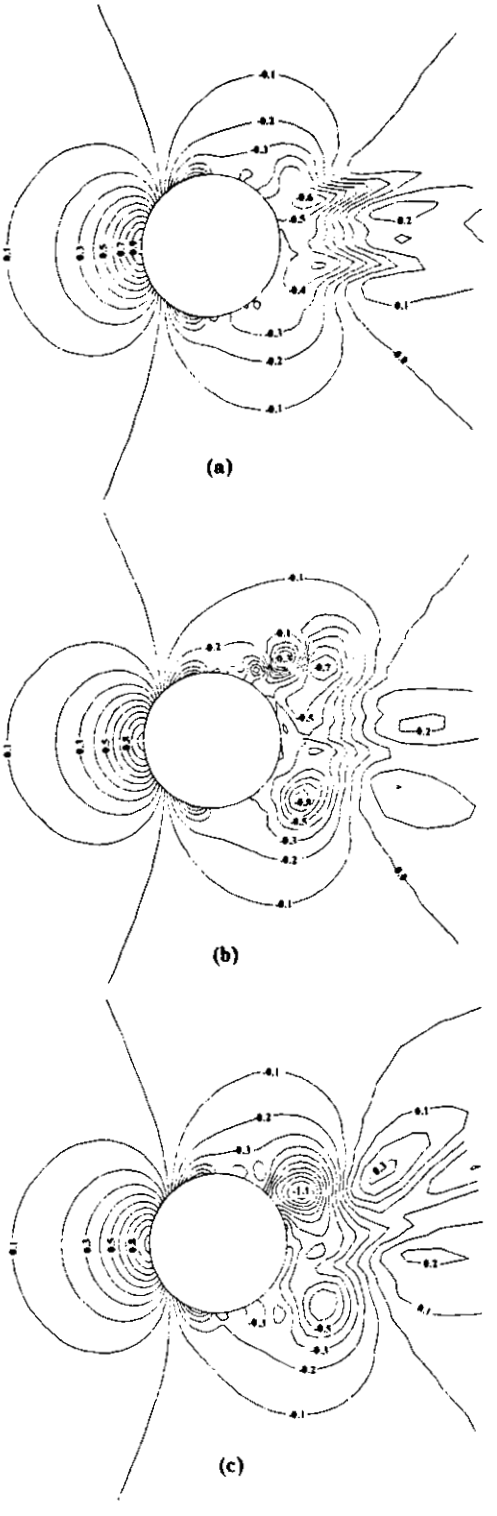

Fig. 3 : Static pressure distributions at different iteration stages in the symmetry plane ($Re_D = 1.62 \cdot 10^5$, Ma = 0.3, laminar flow)

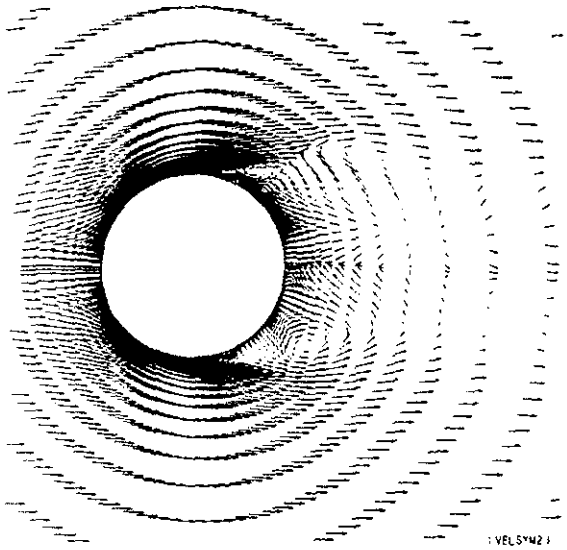

(a)

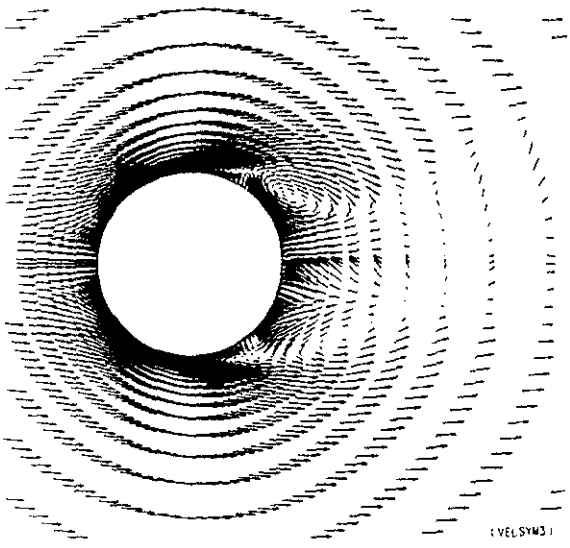

(b)

Fig. 4 : Velocity vector field at different iteration stages in the symmetry plane
($Re_D = 1.62 \cdot 10^5$, Ma = 0.3, laminar flow)

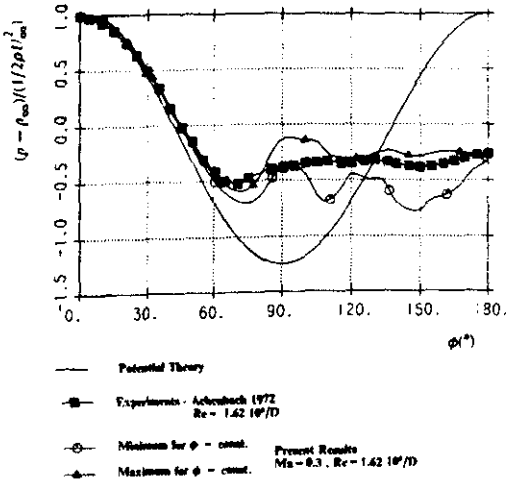

Fig. 5 : Surface pressure as function of angle ϕ
($Re_D = 1.62 \cdot 10^5$, Ma = 0.3, laminar flow),
ϕ measured from front to rear stagnation point

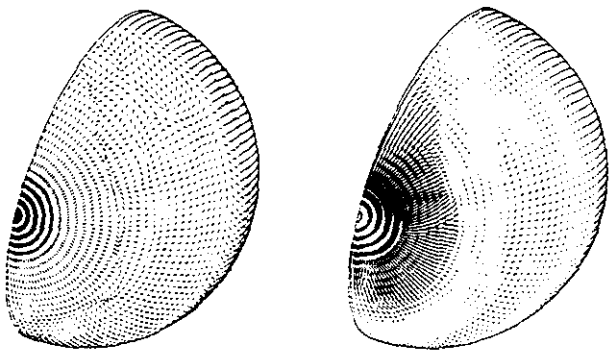

Fig. 6 : Wall stress vectors on sphere rear side
($Re_D = 1.62 \cdot 10^5$, Ma = 0.3, laminar flow),
left: magnitude and direction, right: direction

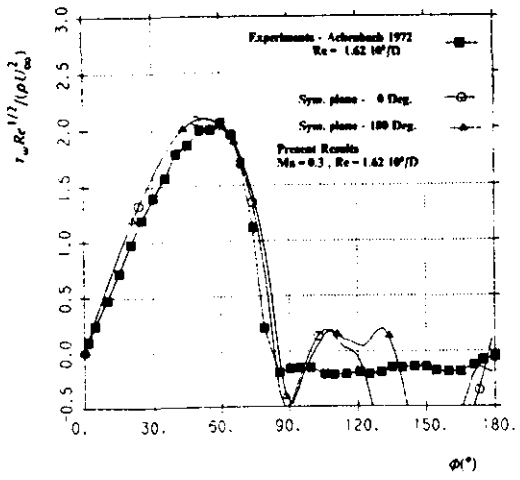

Fig. 7 : Skin-friction as function of angle ϕ
($Re_D = 1.62 \cdot 10^5$, Ma = 0.3, laminar flow),
ϕ measured from front to rear stagnation point

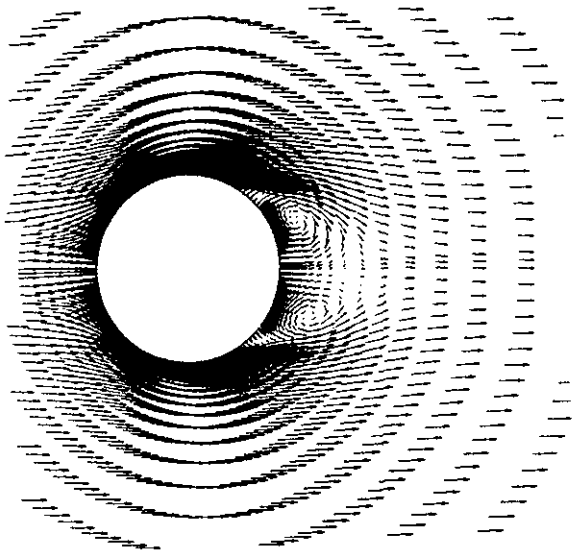

Fig. 9 : Velocity vector field in the symmetry plane
($Re_D = 5 \cdot 10^6$, Ma = 0.1, turbulent flow)

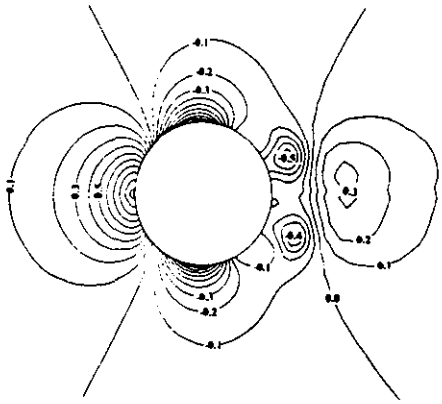

Fig. 8 : Static pressure distributions in the symmetry plane
($Re_D = 5 \cdot 10^6$, Ma = 0.1, turbulent flow)

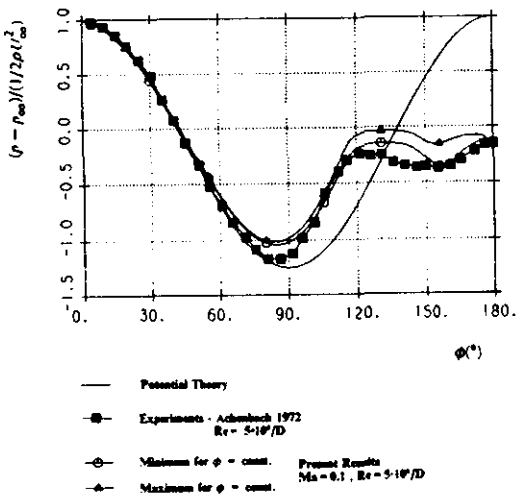

Fig. 10 : Surface pressure as function of angle ϕ
($Re_D = 5 \cdot 10^6$, Ma = 0.1, turbulent flow),
ϕ measured from front to rear stagnation point

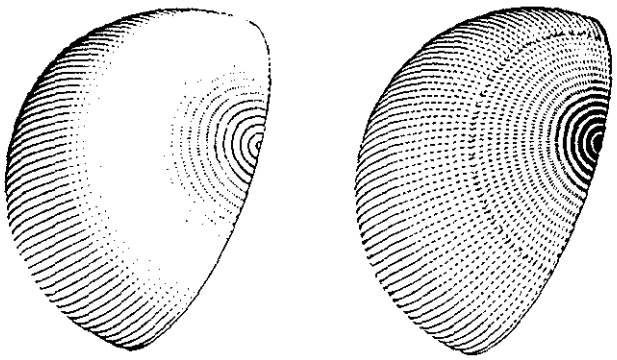

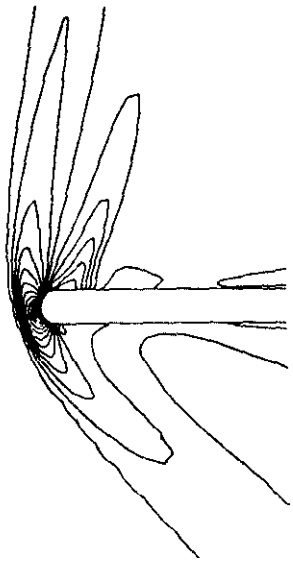

Fig. 11 : Wall stress vectors on sphere rear side
($Re_D = 5 \cdot 10^6$, Ma = 0.1, turbulent flow)
left: magnitude and direction, right: direction

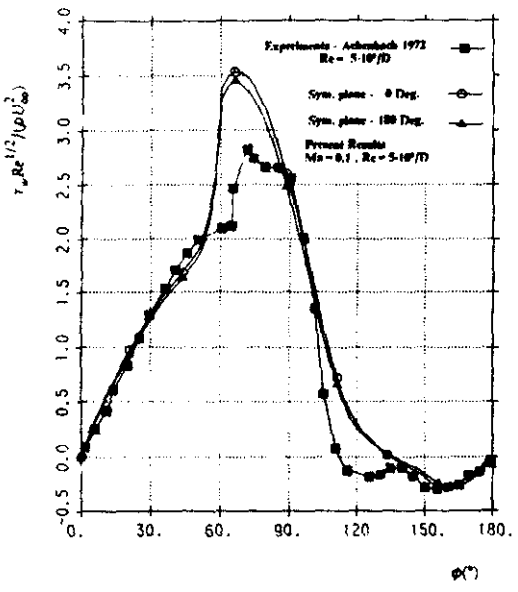

Fig. 12 : Skin-friction as function of angle ϕ
($Re_D = 5 \cdot 10^6$, Ma = 0.1, turbulent flow),
ϕ measured from front to rear stagnation point

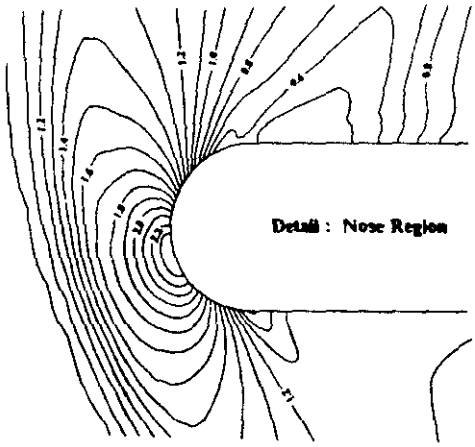

Fig. 13 : Pressure distribution in symmetry plane of hemisphere-cylinder
(Ma = 1.2, $Re_D = 4.45 \cdot 10^5$, $\sigma = 19°$, laminar flow)

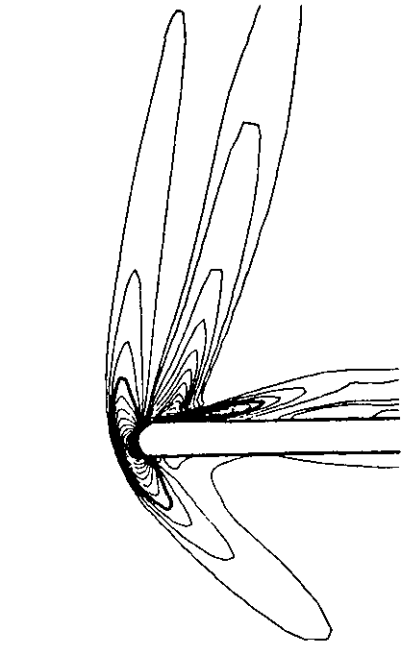

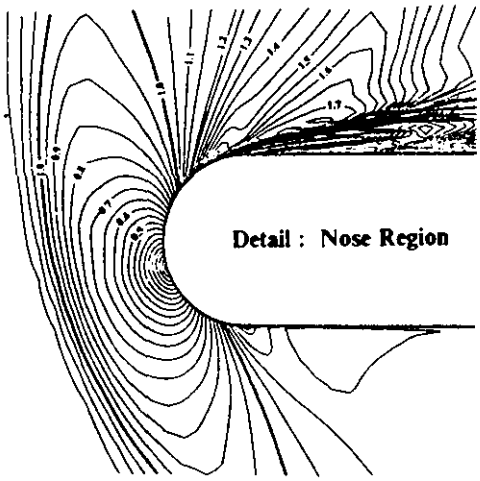

Fig. 14 : Mach number distribution in symmetry plane of hemisphere-cylinder
(Ma = 1.2, Re_D = 4.45·10^5, α = 19°,laminar flow)

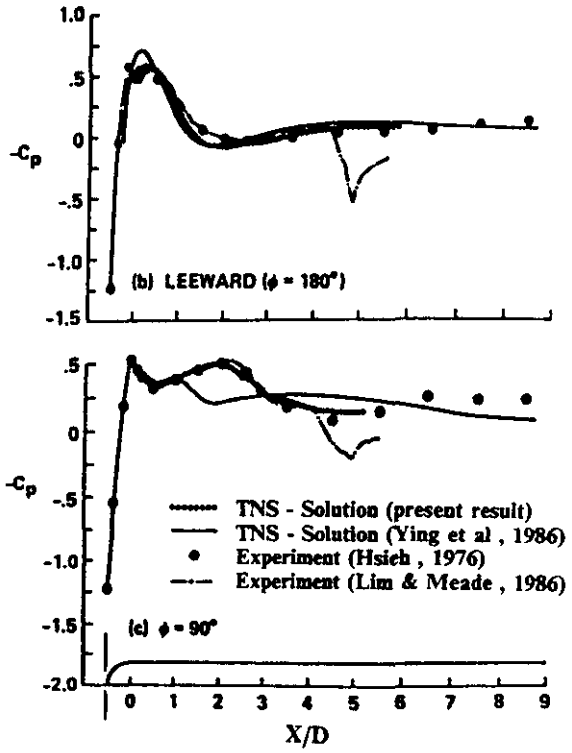

Fig. 15 : Streamwise pressure distribution of hemisphere-cylinder
(Ma = 1.2, Re_D = 4.45·10^5, α = 19°,laminar flow)

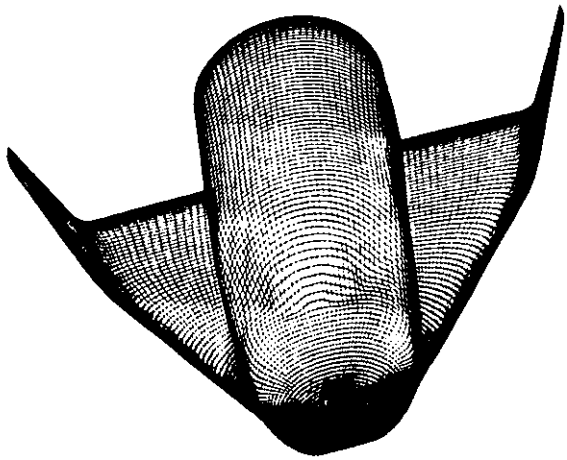

Fig. 16 : Geometry of HERMES space shuttle

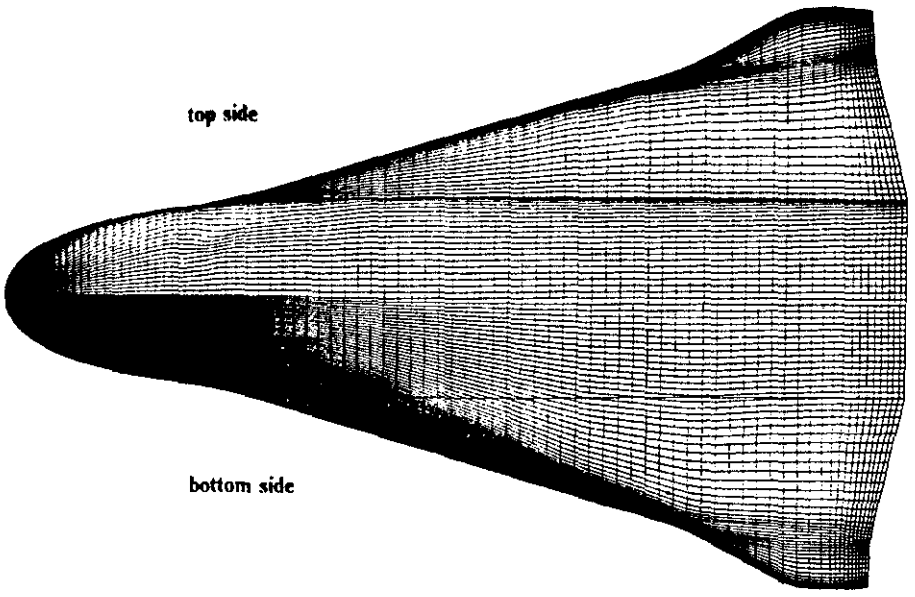

Fig. 17 : Surface mesh for HERMES space shuttle (dimension: 97x129)

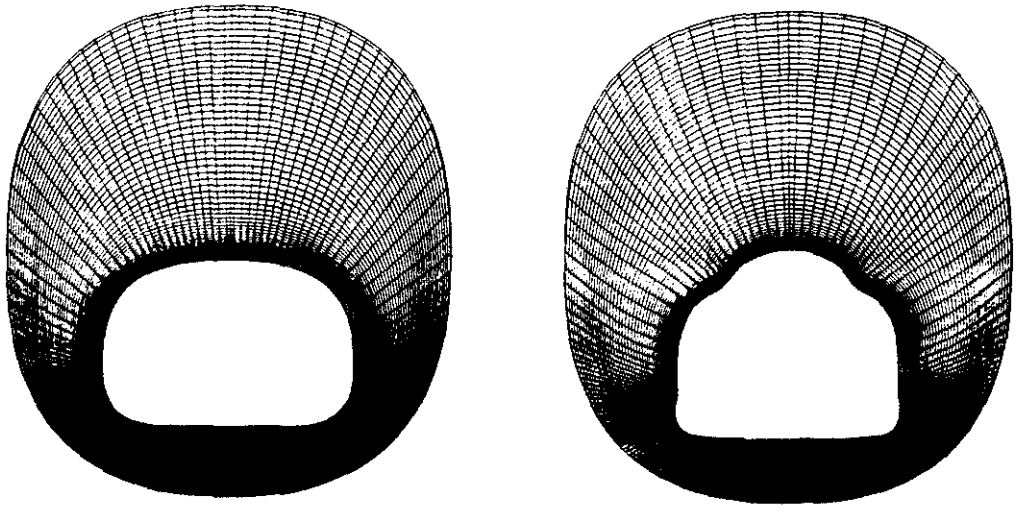

Fig. 18 : Coordinate system in various cross sections x = const.
(dimensions : 129x65)

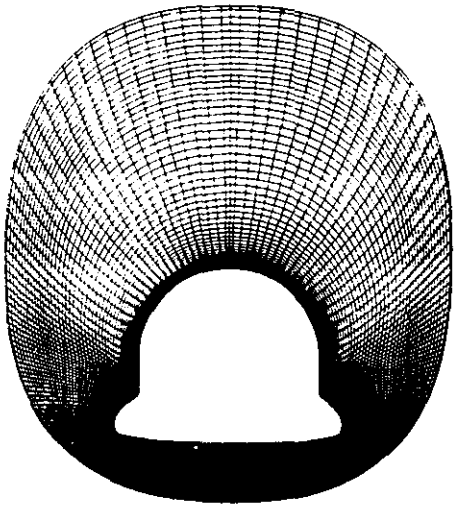

x = 5.6 m

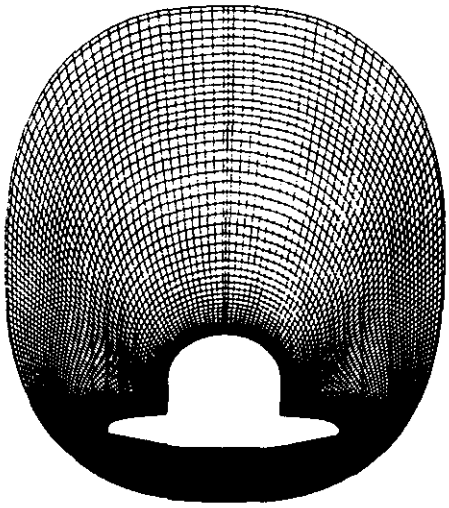

x = 10.0 m

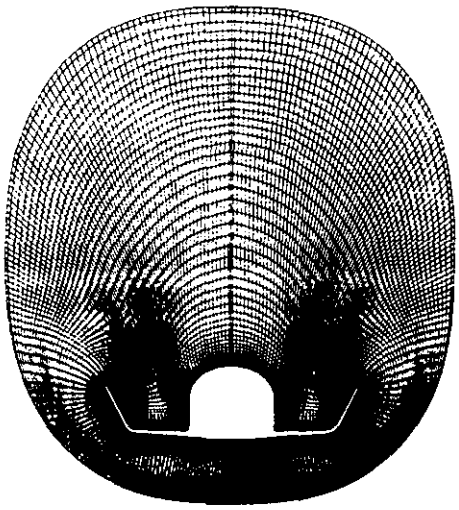

x = 14.8 m

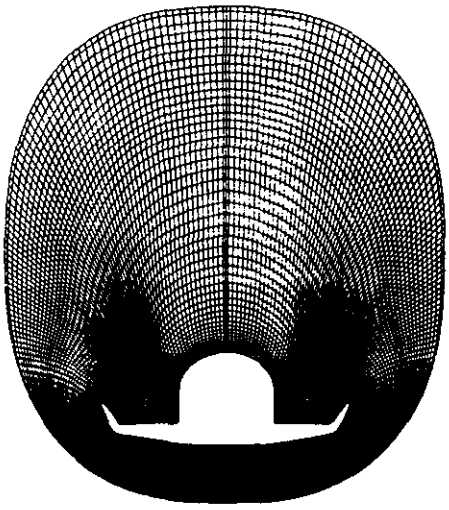

x = 12.7 m

Fig. 18 : (cont.) Coordinate system in various cross sections x = const.
(dimensions : 129x65)

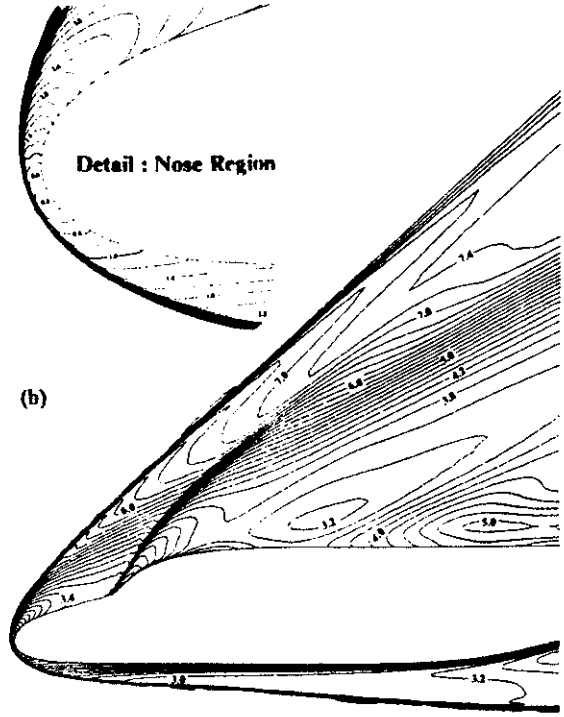

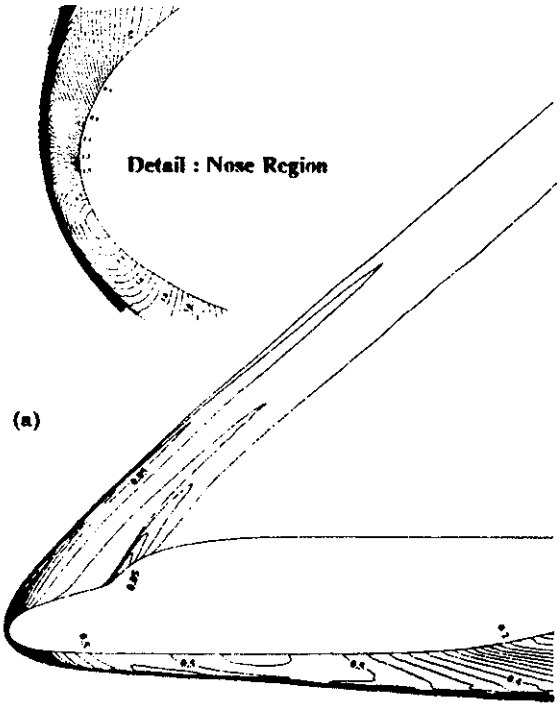

Fig. 19 : Pressure (a) and Mach number (b) distribution in symmetry plane of HERMES space shuttle (Ma = 8 ,α = 30°, inviscid flow)

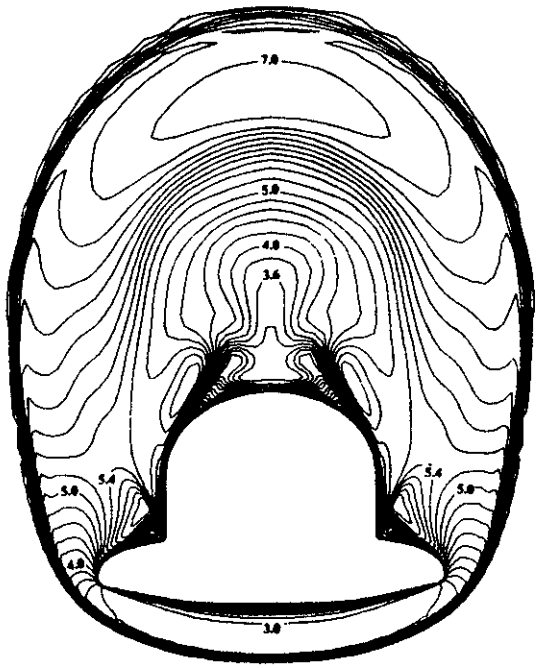

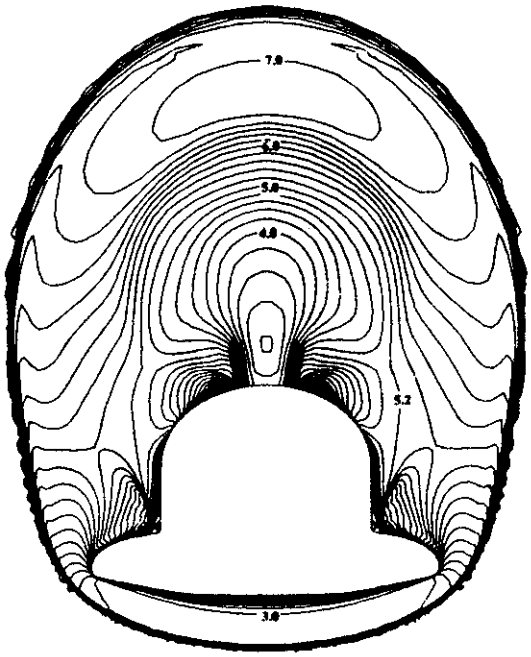

Fig. 20 : Mach number distribution in cross section x = 7.8 m of HERMES space shuttle for viscous (a) and inviscid (b) flow (Ma = 8 , α = 30°, $Re = 10^6/m$)

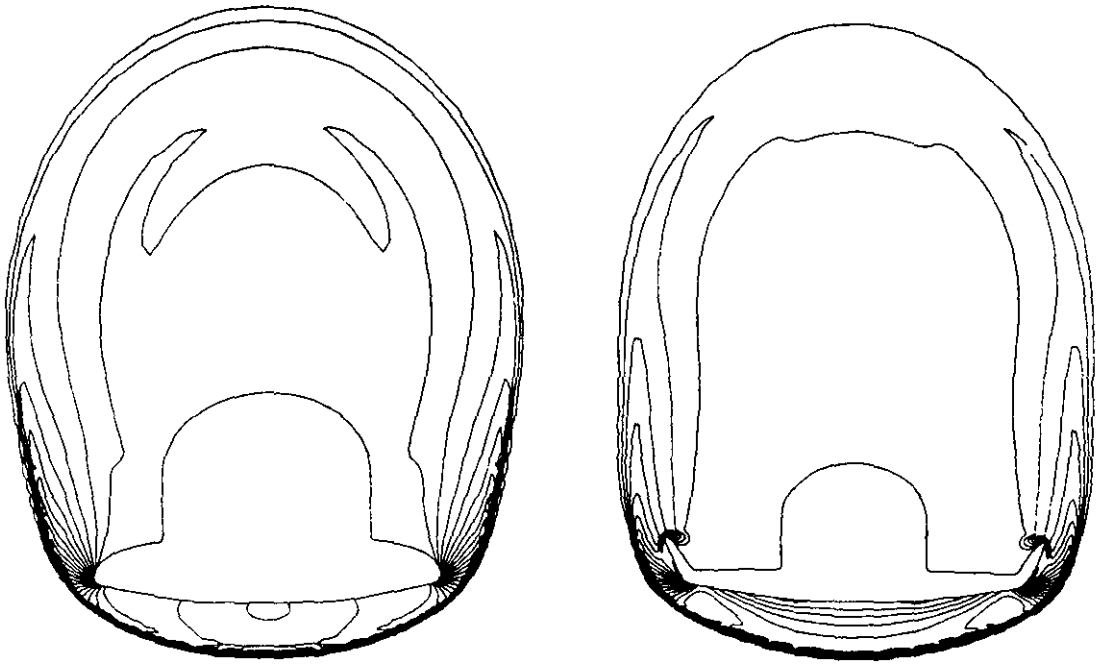

(c) (b)

Fig. 20 : (cont.) Pressure distribution in cross section x = 7.8 m of HERMES space shuttle for inviscid (c) flow
(Ma = 8 , $\alpha = 30°$)

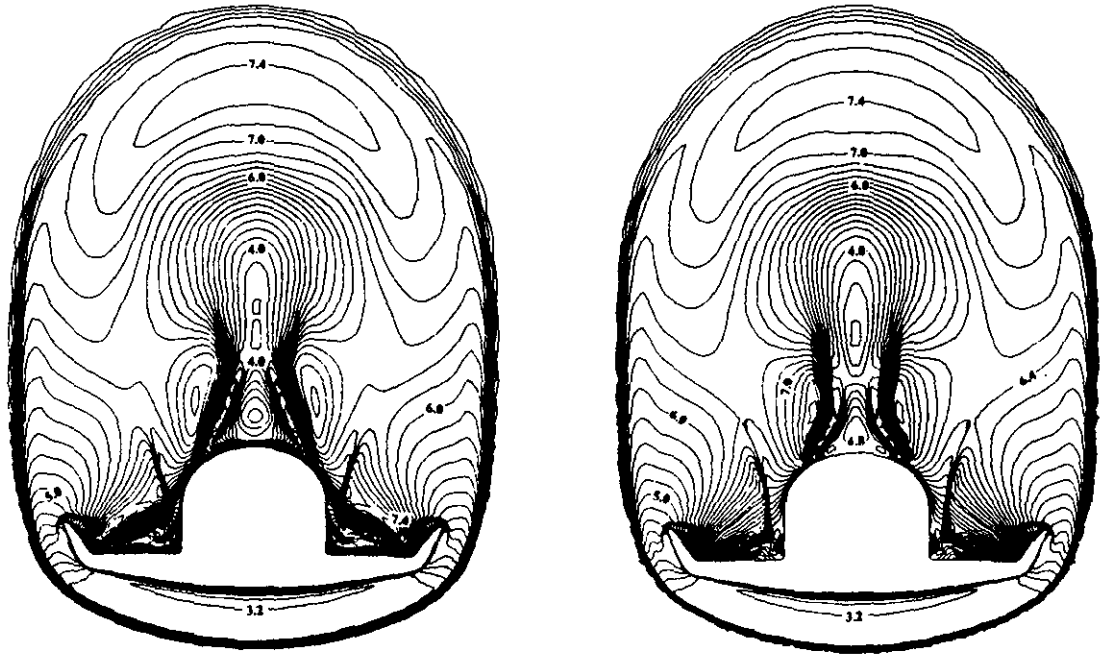

(a) (c)

Fig. 21 : Mach number distribution (a,b) and pressure distribution (c) in cross section x = 12.7 m
of HERMES space shuttle for viscous (a) and inviscid (b,c) flow
(Ma = 8 , $\alpha = 30°$, $Re = 10^6/m$)

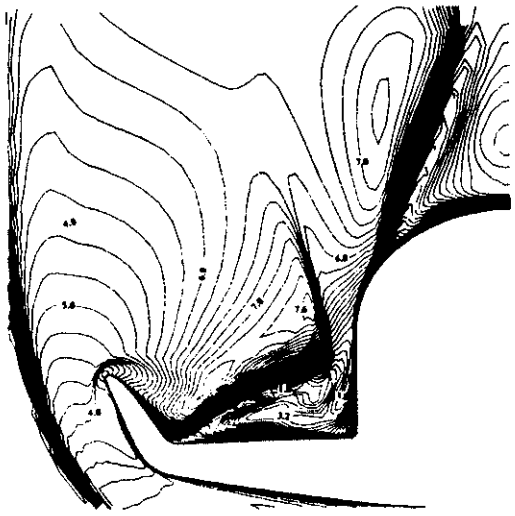

(a)

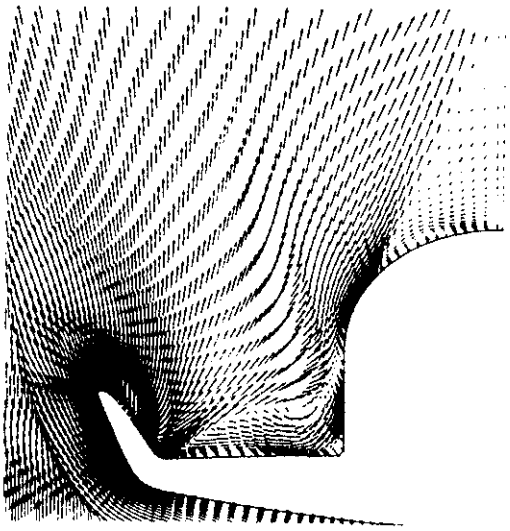

(b)

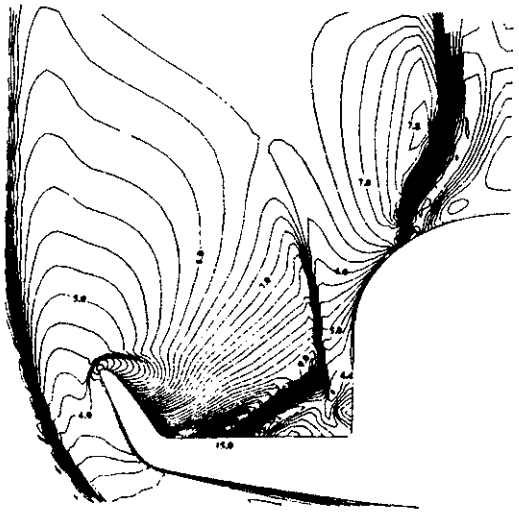

(c)

Fig. 22 : Mach number distribution (a,c) and cross flow velocity field (b) in cross section x = 12.7 m of HERMES space shuttle for viscous (a,b) and inviscid (c) flow
(Ma = 8 , $\alpha = 30°$, $Re = 10^6/m$)

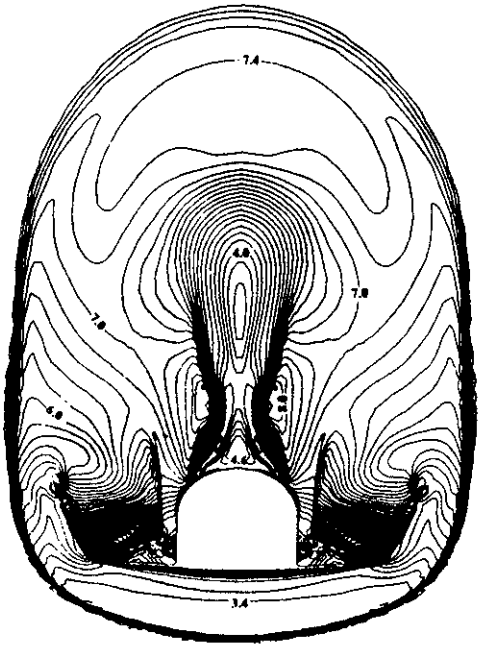

(a)

Fig. 23 : Mach number distribution in cross section x = 15.3 m of HERMES space shuttle for inviscid (a) and viscous (b) flow
(Ma = 8 , $\alpha = 30°$, $Re = 10^6/m$)

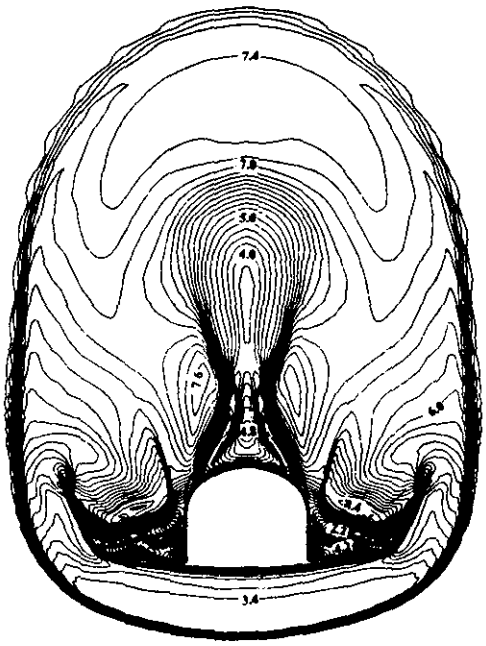

(b)

Fig. 23 : (cont.) Mach number distribution in cross section x = 15.3 m of *HERMES* space shuttle for inviscid (a) and viscous (b) flow
(Ma = 8 , $\alpha = 30°$, $Re = 10^6/m$)

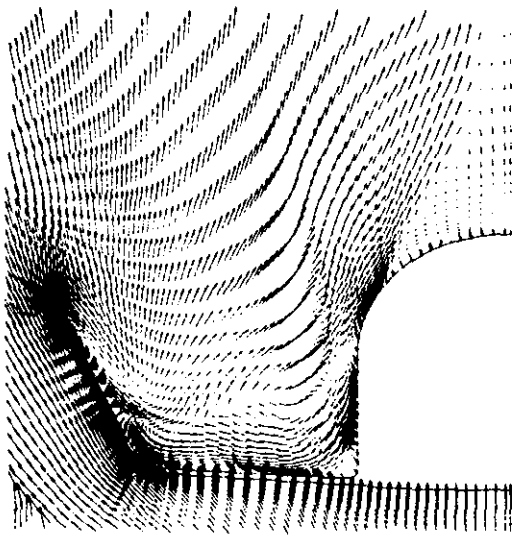

(b)

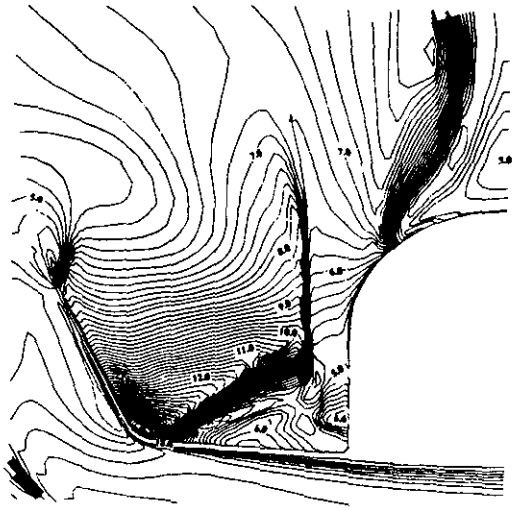

(a)

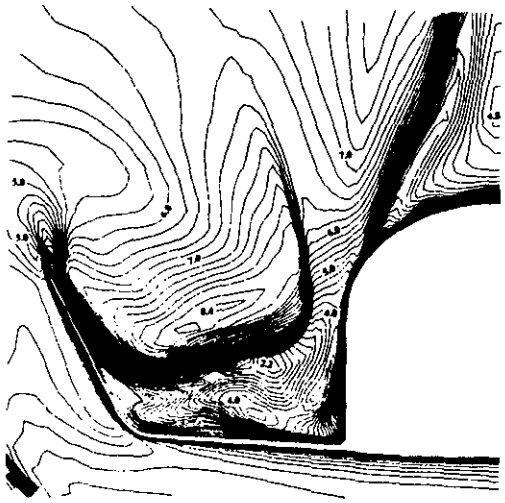

(c)

Fig. 24 : Mach number distribution (a,c) and cross flow velocity field (b) in cross section x = 15.3 m of HERMES space shuttle for viscous (b,c) and inviscid (a) flow
(Ma = 8 , $\alpha = 30°$, $Re = 10^6/m$)

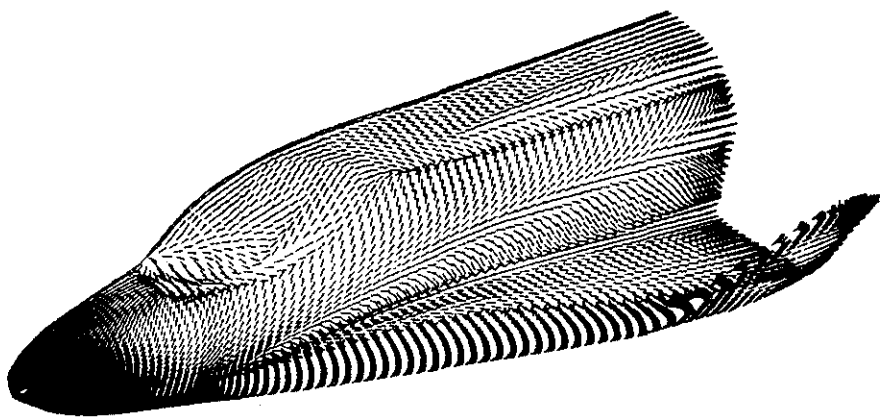

Fig. 25 : Direction of wall stress vectors on HERMES space shuttle
(Ma = 8 , α = 30°, Re = $10^6/m$, laminar flow)